PAPER

WILEY Terra Nova

Garnet-controlled very low velocities in the lower mantle transition zone at sites of mantle upwelling

Thorsten J. Nagel[1] (iD) | Erik Duesterhoeft[2] | Christian Schiffer[3]

[1]Department of Geoscience, Aarhus University, Aarhus, Denmark

[2]Department of Geoscience, Christian-Albrechts University, Kiel, Germany

[3]Department of Earth Sciences, Durham University, Durham, UK

Correspondence
Dr. Thorsten J. Nagel, Department of Geoscience, Aarhus University, Aarhus, Denmark.
Email: thorsten.nagel@geo.au.dk

Abstract

Deep mantle plumes and associated increased geotherms are expected to cause an upward deflection of the lower–upper mantle boundary and an overall thinning of the mantle transition zone between about 410 and 660 km depth. We use subsequent forward modelling of mineral assemblages, seismic velocities, and receiver functions to explain the common paucity of such observations in receiver function data. In the lower mantle transition zone, large horizontal differences in seismic velocities may result from temperature-dependent assemblage variations. At this depth, primitive mantle compositions are dominated by majoritic garnet at high temperatures. Associated seismic velocities are expected to be much lower than for ringwoodite-rich assemblages at undisturbed thermal conditions. Neglecting this ultralow-velocity zone at upwelling sites can cause a miscalculation of the lower–upper mantle boundary on the order of 20 km.

KEYWORDS
660 discontinuity, mantle plume, mantle transition zone, receiver functions, seismic velocity modelling

1 | INTRODUCTION

Hotspot magmatism occurs at sites of convective mantle upwelling. With the time-scale of upward motion short compared to the time-scale of conductive thermal equilibration, mantle material would decompress adiabatically and cross its solidus. Most studies propose a lower mantle source for the rising material (De Paolo & Manga, 2003; Morgan, 1972). Accordingly, the material stream would cross the mantle transition zone (MTZ), the lower part of the upper mantle between about 410 and 660 km depth. The MTZ is bounded by two phase transitions (the 410 and the 660 transitions, respectively), which correspond to considerable density and seismic velocity discontinuities and thus produce large amplitude seismic signals in receiver function (RF) data (e.g., Andrews & Deuss, 2008; Lawrence & Shearer, 2006; Stammler et al., 1992; Vinnik, Kosarev, & Petersen, 1996). The bottom of the MTZ (660 discontinuity) is the boundary between the upper and lower mantle and corresponds to the downward replacement of ringwoodite with periclase plus Mg–Si-perovskite, also called bridgmanite. The top of the MTZ (410 discontinuity)

is defined by the downward replacement of olivine with wadsleyite. The 660 transition has a negative Clapeyron slope while the 410 transition has a positive slope with similar absolute values of 2–3 MPa/K (Deuss, Andrews, & Day, 2013; Gasparik, 2003; Hirose, 2002; Figure 1). The slope of the 660 transition is actually controversial with some estimates as high as −1 MPa/K. Most experiments, first-principle calculations and fundamental seismic studies (e.g., Hernández, Brodholt, & Alfè, 2015; Hirose, 2002; Tauzin & Ricard, 2014; Yu, Wentzcovitch, Tsuchiya, Umemoto, & Weidner, 2007), however, point to values lower than −2 MPa/K (Cottaar & Deuss, 2016). Because of the opposite slopes of the bounding reactions, the MTZ should become thinner with increasing geothermal gradients (Bina & Helffrich, 1994). Yet, observations at hotspot sites have been ambiguous. While the 410 discontinuity typically does show the expected downward excursion, the behaviour of the 660 discontinuity is less consistent. In Iceland, Jenkins, Cottaar, White, and Deuss (2016) found the bottom of the MTZ displaced downward and attributed this to a garnet-related positive Clapeyron slope at high temperatures. Recent RF data from Hawaii show overall

moderate topography of the 660 discontinuity with upward and downward displacements (Agius, Rychert, Harmon, & Laske, 2017; see also Cao, van der Hilst, de Hoop, & Shim, 2011). Similar observations exist from the East African Rift (e.g., Cornwell, Hetényi, & Blanchard, 2011; Huerta, Nyblade, & Reusch, 2009), the Western US (Gao & Liu, 2014), and South China (Huang, Tosi, Chang, Xia, & Qiu, 2015). We present progressive forward modelling of mineral assemblages (Figures 1 and 2), seismic velocities (Figure 3), and 1D RFs (Figures 4 and 5) along various adiabats. Assemblage evolutions are similar for different adiabats except for the lower MTZ where garnet-rich assemblages may cause a pronounced low-velocity anomaly for hot geotherms. This low-velocity zone would account for larger-than-expected delay times at hotspot sites, which may lead to artificial deepening of the 660 discontinuity in seismic observations, if unaccounted for in time–depth conversions.
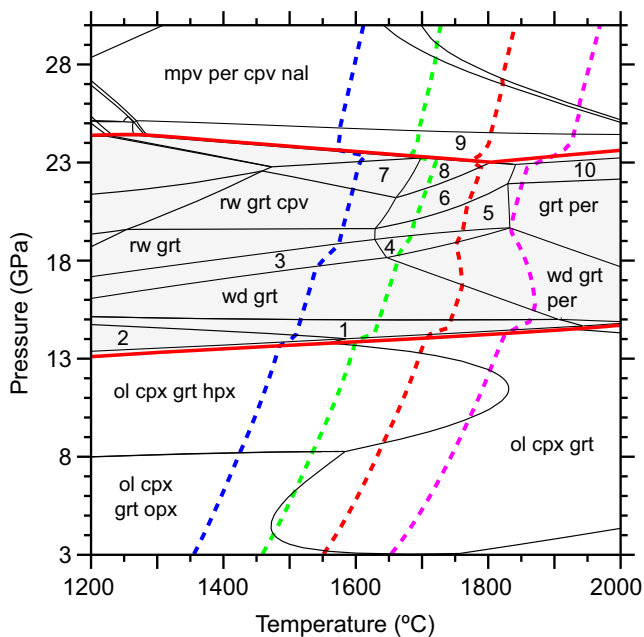

FIGURE 1 Equilibrium phase diagram for a primitive mantle composition (Lyubetskaya & Korenaga, 2007). Molar abundances of elements in simplified bulk composition used for the calculation are: Si, 38.34; Al, 3.51; Fe, 5.64; Mg, 49.80; Ca, 2.53; Na, 0.49; O, 139.200. Red lines and shaded area highlight the mantle transition zone. Dashed lines are isentropes representing adiabatic geotherms defined by potential temperatures of 1,350°C (blue), 1,450°C (green), 1,550°C (red), and 1,650°C (pink) at 3 GPa respectively. Mineral abbreviations are: cfe, Ca-ferrite; cpv, Ca–Si-perovskite; cpx, clinopyroxene; grt, garnet; hpx, high-pressure polymorph of opx; mpv, Mg–Si-perovskite (bridgmanite); nal, NAL phase (Mookherjee, Karki, Stixrude, & Lithgow-Bertelloni, 2012); ol, olivine; opx, orthopyroxene; per, periclase; rw, ringwoodite; wd, wadsleyite. Assemblages: 1, wd + grt + cpx; 2, wd + grt + cpx + hpx; 3, wd + rw + grt; 4, wd + rw + grt + per; 5, rw + grt + per; 6, rw + grt + per + cpv; 7, rw + grt + cpv + nal; 8, rw + grt + cpv + nal + per; 9, mpv + grt + cpv + nal + per; 10, grt + per + cpv. See text for more calculation details

2 | MODELLING PHASE RELATIONS, SEISMIC VELOCITIES, AND RECEIVER FUNCTIONS

The emergence of thermodynamic databases allowing for quantitative modelling of assemblages at mantle conditions (Holland, Hudson, Powell, & Harte, 2013; Stixrude & Lithgow-Bertelloni, 2011) has provided a powerful tool to study mantle processes and their seismic footprints (e.g., Cammarano, 2013; Shorttle, Mavlennan, & Lambart, 2014; Stixrude & Lithgow-Bertelloni, 2012; Xu, Lithgow-Bertelloni, Stixrude, & Ritsema, 2008). We use Theriak/Domino software (De Capitani & Petrakakis, 2010) and the database from Holland et al. (2013) to explore phase relations in primitive mantle (Figure 1). The composition employed here is from Lyubetskaya and Korenaga (2007). Other common propositions yield almost identical phase relations (Supporting Information, Figure S1). Along with the thermodynamic calculations come density, entropy, and Gibbs free energy, which are further utilized in the subsequent modelling. Adiabats shown in Figure 1 are calculated from the entropy of the predicted stable mineral assemblages and used to approximate primitive mantle geotherms down to 800 kilometres depth (30 GPa) for potential temperatures of 1,350°C, 1,450°C, 1,550°C, and 1,650°C (at 3 GPa) respectively. Synthetic profiles of seismic velocities (Figures 2 and 3b) are derived from assemblages, using the Theriak_D add-on (Duesterhoeft & de Capitani, 2013). We used a novel heuristic technique for calculating the shear modulus needed for computation of seismic velocities as a function of temperature, pressure, and composition (see supporting information for a detailed description).

The RF method is a common tool to image seismic discontinuities, traditionally in the crust and upper mantle, by deconvolving waveforms of incident teleseismic P-waves that are converted to S-waves (e.g., Ammon, 1991; Kind, Kosarev, & Petersen, 1995; Langston, 1979; Vinnik, 1977). The P-to-S conversions are visualized as pulses at the delay time of the converted S-wave after the P-wave. This delay time is dependent on the depth of the discontinuity, the overlying S- and P-wave velocity structure and the ray parameter (Zhu & Kanamori, 2000). A RF with known parameters of an incident earthquake may thus be back-migrated from delay time to the true conversion point, if the overlying velocities are known, while usage of a wrong velocity model may lead to errors in depth (Tauzin & Ricard, 2014). We produce synthetic 1D RFs of the thermodynamically estimated velocity–density models, which are initially translated from pressure to depth. These synthetic MTZ images are idealized, perfectly depth-migrated and noise-free. Real data would be obscured by noise, scattering, and imaging artefacts. However, the target of this study was to identify first-order characteristics of the time–depth migration of major discontinuities and the effect of velocity models. These effects will show robustly in real data. The pressure–depth conversion in our modelling assumes a lithostatic depth defined by density-integration along the 1,350°C adiabat and extended by a standard continental lithosphere at the top (35 km thick crust with a density of 2,800 kg/m^3 and 100 km thick lithospheric mantle with a density of 3,300 kg/m^3). Hence, we assume
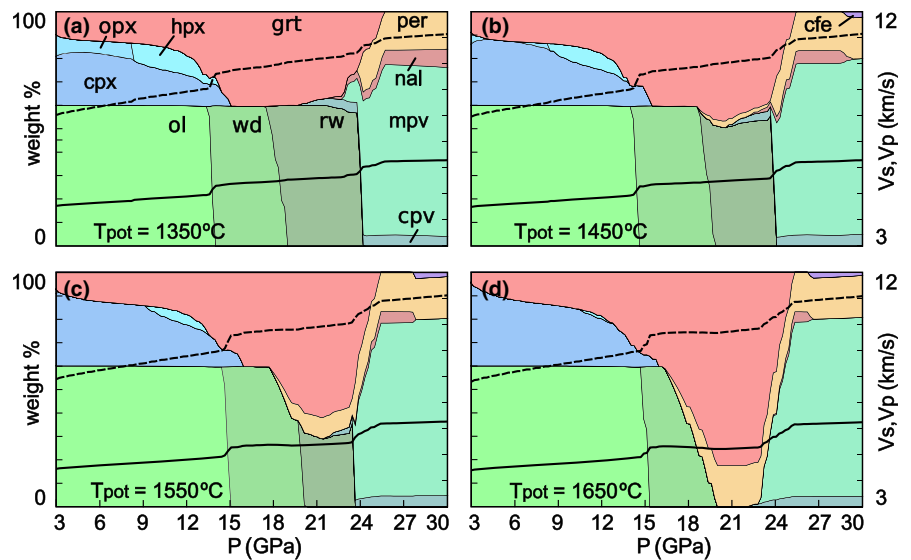
FIGURE 2 Assemblages along four adiabats displayed in Figure 1. Figure 2a–d correspond to 1,350, 1,450, 1,550, and 1,650 adiabats respectively. Dashed and solid black lines show velocities of P- and S-waves respectively. Mineral abbreviations are the same as in Figure 1
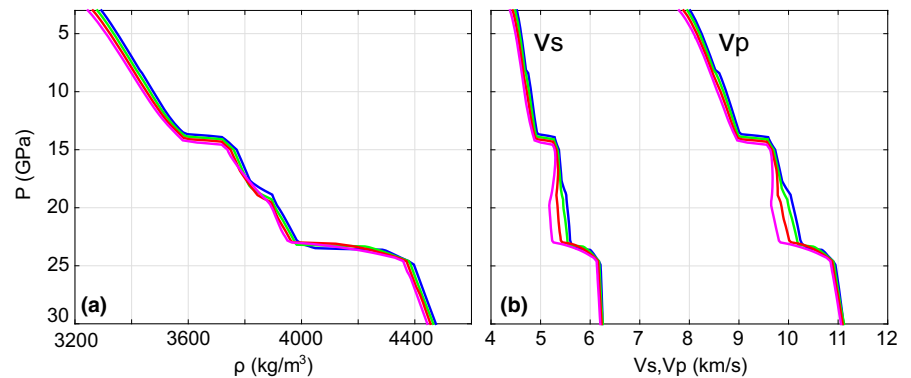

FIGURE 3 Calculated densities (a) and velocities of P- and S-waves (b) along the 1,350 (blue), 1,450 (green), 1,550 (red), and 1,650 (pink) adiabats respectively Figure 1. See Supporting Information Data S1 for calculation details

pressure equilibrium between upwelling and ambient mantle. Synthetic RFs are calculated using the velocity–density–depth profiles (Supporting Information, Figure S2) and a 1D wavefield code to compute the surface response to an incoming plane wave (Kennet, 1983) and subsequent waterlevel-deconvolution with a Gaussian factor of 2 (e.g., Clayton & Wiggins, 1976; Langston, 1979) (Supporting Information, Figure S3 shows the effect of different Gaussian filters). As for real RFs, the synthetics are given in delay time (Figure 4a). The lithospheric layers are removed and constant lithospheric velocities (V_s = 4.5 km/s, V_p = 8.1 km/s) are assumed in the upper 135 km to obtain MTZ signals undisturbed by multiple conversions (Supporting Information, Figure S4 shows the negligible effect of multiples). Thereafter, the RFs are converted to depth (Figure 4b).

3 | RESULTS

Figure 1 shows the classic phase transitions bordering the MTZ, i.e., the 410 and the 660 discontinuities. Narrowing of the MTZ with increasing temperature is predicted to occur up to 1,800°C, where the slope of the 660 transition becomes positive. This slope change reflects the changeover from the assemblage ringwoodite/

wadsleyite + garnet + Ca–Si-perovskite to majorite-rich garnet + periclase, which takes place towards high temperatures in the MTZ. The associated reactions are continuous and may start below 1,650°C at 20 GPa. Figure 2 displays predicted assemblage evolutions and seismic velocities following adiabats in Figure 1. The above-described reaction represents by far the most significant difference in assemblage evolution between normal and high-temperature scenarios. At pressures below 16 GPa and above 24 GPa, assemblages evolve similarly. In the lower MTZ, however, majoritic garnet + periclase progressively replace Mg_2SiO_4 phases towards higher temperatures. This leads to the complete disappearance of ringwoodite at 20 GPa along the 1,650°C adiabat. The horizontal mineralogical variation in the lower MTZ is associated with a significant reduction in velocity (Figures 2–4). While below and above the MTZ, temperature-dependent velocity differences would be in the order of the typical tomographic signal, i.e., 1%–1.5%, velocities in the lower MTZ display a pronounced fanning with differences up to about 7% for S-waves and 5% for P-waves (Figure 3b). Figure 4 shows synthetic RFs. The 410 and 660 discontinuities produce the expected large amplitude positive conversion signals. The 410 discontinuity shows a clear deepening with higher temperatures. The 660 discontinuity displays less pronounced depth differences
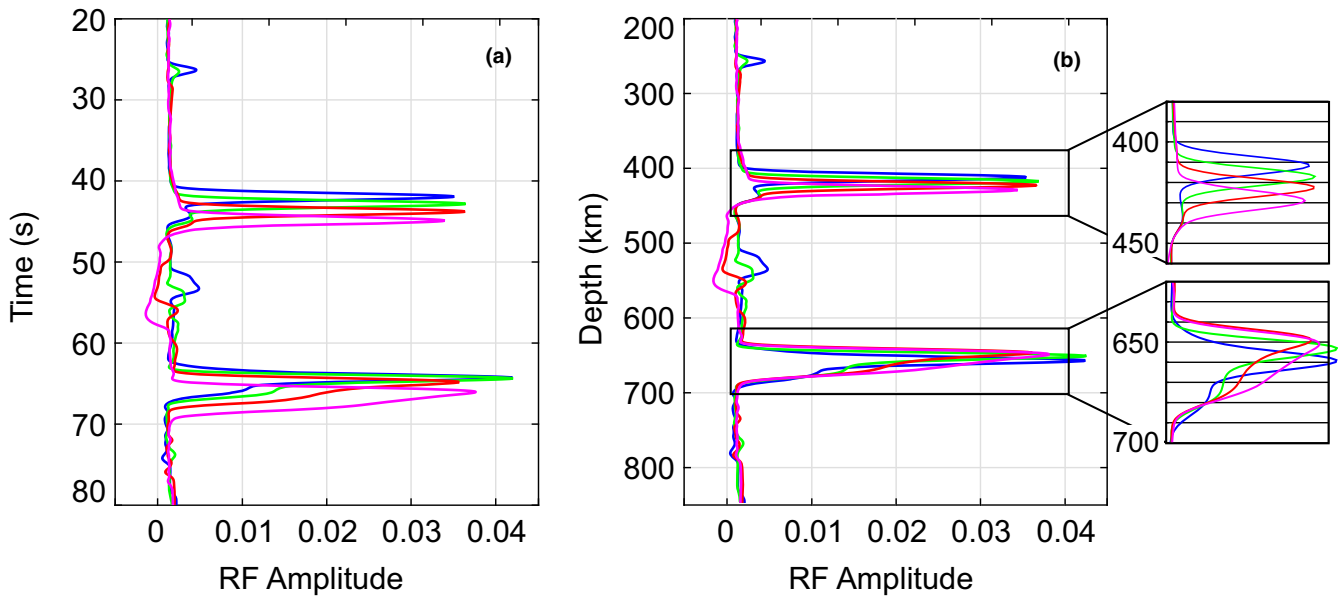
FIGURE 4 Modelled receiver function (RF) signals along the 1,350 (blue), 1,450 (green), 1,550 (red), and 1,650 (pink) adiabats respectively (Figure 1). (a) RFs versus delay time calculated from the depth-converted models from Figure 3b (Supporting Information Figure S2). (b) RFs versus depth back-migrated from delay times in Figure 4a. Insets highlight RF signals bounding the mantle transition zone. The transition zone thicknesses for different adiabats are 247 km (1,350, blue), 237 km (1,450, green), 228 km (1,550, red), and 224 km (1,650, pink). The delay time differences between the 410 and 660 discontinuities are 22.7 s (1,350, blue), 21.9 s (1,450, green), 21.45 s (1,550, red), and 21.7 s (1,650, pink)
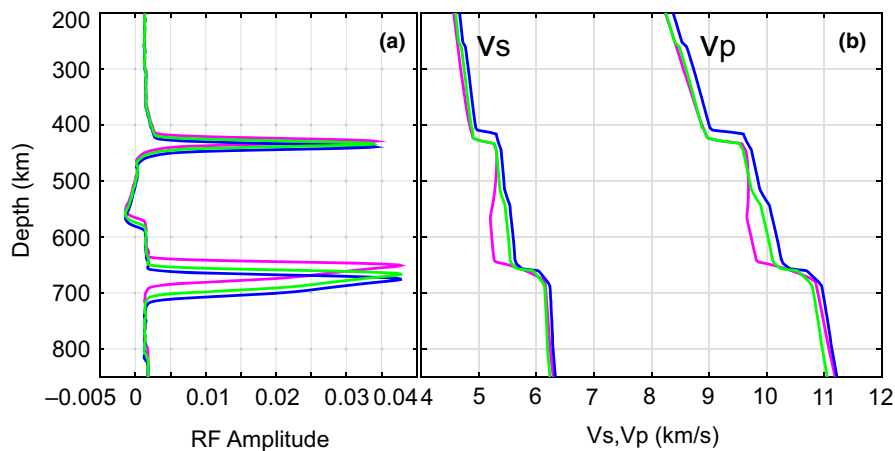

FIGURE 5 Depth-converted RF signals for the 1,650 adiabat from Figure 4a (a) using three different velocity–depth models for depth conversion (b) Pink: velocity model of the 1,650 adiabat placing RF signals at the proper depth (true model). Blue: Velocity model of the 1,350 adiabat, yielding predictions too deep because of the higher velocities. Green: Velocity model of the 1,350 adiabat assuming a general velocity reduction of 1.5% and a corrected depth of the 410 transition, still yielding a prediction around 17 km too deep for the 660 discontinuity as the low-velocity zone in the lower mantle transition zone is not accounted for. The transition zone thicknesses for the three models are 224 km (pink), 231 km (green), and 241 km (blue)

although the negative pressure–temperature slope has similar amplitude. Because of higher densities in the lowermost MTZ compared to the top of the MTZ, the depth–temperature slope of the 660 transition is diminished. Also, the assemblage and property change across the 660 transition is distributed over a depth range of 30 km resulting in a more diffuse signal compared to the 410 discontinuity, which spreads over a depth interval of only 10 km (Figure 3b). The

1,650°C adiabat cuts the 660 transition above 1,800°C, where the Clapeyron slope has turned positive and the RF signal starts to deepen again (Figures 1 and 4b). The wadsleyite–ringwoodite transition (often called the 520 transition) produces a small positive conversion along the 1,350°C adiabat. At elevated temperatures, the phase-change-related decrease of velocities with depth results in a low-amplitude negative conversion signal at 530–580 km depth. This

signal, both as a positive and negative 520 discontinuity, might be challenging to resolve in real data; the impact of the low-velocity layer on delay times, however, is robust and momentous.

The MTZ is predicted to show only minor shortening of the delay time width with increasing temperature (Figure 4a). The depth difference of the 660 discontinuity between the 1,350 and the 1,550 adiabat is outweighed by the velocity difference in the lower MTZ, causing a larger delay time for warmer adiabats (Figure 4a). Although the 660 discontinuity is 8 km shallower along the 1,650°C than along the 1,350°C adiabat (Figure 4b), its delay time is 1.8 s longer. Figure 5 illustrates the effects of the low-velocity zone in the lower MTZ on the inferred depth of the 660 discontinuity using different velocity models for time–depth conversion. Using the velocity model of the 1,350°C adiabat to convert the RFs of the 1,650°C adiabat (Figure 4a) leads to a 660 discontinuity estimation 26 km too deep. Even if a general temperature-related velocity reduction of 1.5% - the typical magnitude inferred in tomographic models - is assumed and the model is corrected for the altered location of the 410 discontinuity (Figure 5b), the 660 discontinuity is still placed 17 km too deep.

4 | DISCUSSION

Some recent studies have used compositional variations to explain the seismic signature of different tectonic environments (e.g., Adam, Caddick, & King, 2017; Maguire, Ritsema, & Goes, 2017). A rising plume, however, cannot carry more than 10% of dense MORB and should mainly consist of primitive mantle material (Brown & Lesher, 2015; Shorttle et al., 2014). Accordingly, the seismic signature of a plume would essentially be that of primitive mantle and we propose that the riddle of the little affected MTZ thickness below hotspots can be solved following that assumption. Our explanation rests on two keystones: the discussed temperature-dependent phase change in the lower MTZ and the comparatively low seismic velocities of Mg-rich, majoritic garnet. Both these essentials have been robustly confirmed in experimental and theoretical studies. The decay of ringwoodite to form majorite component and periclase is well-known in experimental petrology. In a pyrolite composition, it takes place between about 1,650°C and 1,800°C at pressures of 20–23 GPa (e.g., Deuss et al., 2013; Gasparik, 2003; Hirose, 2002; Ishii, Kojitani, & Akaogi, 2011). More enriched compositions show the reaction even at slightly lower temperatures (Supporting Information, Figures S1 and S5). The other keystone, a high Poisson's ratio and associated low seismic velocities of majoritic garnet compared to ringwoodite, is also well established in experimental work and theoretical modelling (e.g., Sinogeikin, Bass, Kavner, & Jeanloz, 1997; Sinogeikin & Bass, 2002; Irifune et al., 2008; Liu et al., 2016; Chantel et al., 2016). Using other approaches, i.e., the database from Stixrude and Lithgow-Bertelloni (2011) together with Perplex software (Connolly, 2005), likewise yields the phase-change-related and characteristic fanning of velocities in the lower MTZ (Supporting Information, Figures S6, S7, S8, S9, see also Xu et al., 2008).

Our velocity modelling predicts an S-wave anomaly of up to 7% for warm adiabats (1,650°C). Due to limited resolution and ray coverage, such a velocity anomaly might not be seen as pronounced and confined in tomographic images as a forward model would suggest. In the recent paper of Maguire et al. (2017), the forward computed velocity models of various plume scenarios do suggest low velocities in the lower MTZ; however, the inverse tomographic image fails to recover the vertical extent of these layers. Velocity models based on tomographic results alone might thus be insufficient.

The 520 discontinuity on top of the lower MTZ is an elusive boundary which may display negative or positive signals, double peaks, or may even be absent (e.g., Andrews & Deuss, 2008; Chevrot, Vinnik, & Montagner, 1999; Deuss et al., 2013; Huang et al., 2015). A low-velocity anomaly in the lower MTZ at mantle-upwelling sites has been proposed in several studies based on negative conversions in RF data. Shen and Blum (2003) observed a negative conversion between 570 and 600 km depth in South Africa and subsequently at several other sites (Shen, Yuan, & Li, 2014). Vinnik, Foulger, and Du (2005) found a negative conversion at a depth of about 500 km around Iceland and four other hotspot locations (Vinnik & Farra, 2006). These observations were attributed to MORB material possibly accumulated in the lower MTZ (Shen et al., 2014) or dehydration melting during heating of water-saturated wadsleyite in the lower MTZ (Vinnik & Farra, 2006). However, MORB would be abundant in Fe-rich garnet with properties very different from majorite-rich garnet in primitive mantle. In modelling, it consistently yields higher velocities than the surrounding mantle in the MTZ (e.g., Shorttle et al., 2014). Also, plumes from the lower mantle are expected to be relatively dry. An explanation by means of elevated temperatures and Mg-rich majoritic garnet in primitive mantle offers a simple and elegant alternative explanation for negative conversions observed in the MTZ.

ORCID

Thorsten J. Nagel iD http://orcid.org/0000-0001-6158-4052

REFERENCES

Adam, C., Caddick, M. J., & King, S. D. (2017). Pyroxenite causes fat plumes and stagnant slabs. *Geophysical Research Letters*, *44*, 4730–4737. https://doi.org/10.1002/2017GL072943

Agius, M. R., Rychert, C. A., Harmon, N., & Laske, G. (2017). Mapping the mantle transition zone beneath Hawaii from Ps receiver functions: Evidence for a hot plume and cold mantle downwellings. *Earth and Planetary Science Letters*, *474*, 226–236. https://doi.org/10.1016/j.epsl.2017.06.033

Ammon, C. J. (1991). The isolation of receiver effects from teleseismic P waveforms. *Bulletin of the Seismological Society of America*, 81, 2504–2510.

Andrews, J., & Deuss, A. (2008). Detailed nature of the 660 km region of the mantle from global receiver function data. *Journal of Geophysical Research: Solid Earth*, 113, B06304. https://doi.org/10.1029/2007JB005111

Bina, C. R., & Helffrich, G. (1994). Phase transition Clapeyron slopes and transition zone seismic discontinuity topography. *Journal of Geophysical Research*, 99(B8), 15853–15860. https://doi.org/10.1029/94JB00462

Brown, E. L., & Lesher, C. E. (2015). North Atlantic magmatism controlled by temperature, mantle composition and buoyancy. *Nature Geoscience*, 7, 820–824.

Cammarano, F. (2013). A short note on the pressure-depth conversion for geophysical interpretation. *Geophysical Research Letters*, 40, 4834–4838. https://doi.org/10.1002/grl.50887

Cao, Q., van der Hilst, R. D., de Hoop, M. V., & Shim, S.-H. (2011). Seismic imaging of transition zone discontinuities suggests hot mantle west of Hawaii. *Science*, 332, 1068–1071. https://doi.org/10.1126/science.1202731

Chantel, J., Manthilake, G. M., Frost, D. F., Beyer, C., Boff a Ballaran, T., Jing, Z., & Wang, Y. (2016). Elastic wave velocities in polycrystalline Mg3Al2Si3O12-pyrope garnet to 24 GPa and 1300 K. *American Mineralogist*, 101, 991–997.

Chevrot, S., Vinnik, L., & Montagner, J.-P. (1999). Global-scale analysis of the mantle Pds phases. *Journal of Geophysical Research*, 104, 20203–20219. https://doi.org/10.1029/1999JB900087

Clayton, R. W., & Wiggins, R. A. (1976). Source shape estimation and deconvolution of teleseismic bodywaves. *Geophysical Journal of the Royal Astronomical Society*, 47, 151–177. https://doi.org/10.1111/j.1365-246X.1976.tb01267.x

Connolly, J. A. D. (2005). Computation of phase equilibria by linear programming: A tool for geodynamic modelling and its application to subduction zone decarbonation. *Earth and Planetary Science Letters*, 236, 524–541. https://doi.org/10.1016/j.epsl.2005.04.033

Cornwell, D. G., Hetényi, G., & Blanchard, T. D. (2011). Mantle transition zone variations beneath the Ethiopian Rift and Afar: Chemical heterogeneity within a hot mantle? *Geophysical Research Letters*, 38, L16308. https://doi.org/10.1029/2011GL047575

Cottaar, S., & Deuss, A. (2016). Large-scale mantle discontinuity topography beneath Europe: Signature of akimotoite in subducting slabs. *Journal of Geophysical Research: Solid Earth*, 121, 279–292. https://doi.org/10.1002/2015JB012452

De Capitani, C., & Petrakakis, K. (2010). The computation of equilibrium assemblage diagrams with Theriak/Domino software. *American Mineralogist*, 95, 1006–1016. https://doi.org/10.2138/am.2010.3354

De Paolo, D. J., & Manga, M. (2003). Deep Oroigin of Hotspots—The Mantle Plume Model. *Science*, 300, 920–921.

Deuss, A., Andrews, J., & Day, E. (2013). Seismic observations of mantle discontinuities and their mineralogical and dynamical interpretation. In S.-I. Karato (Ed.), *Physics and Chemistry of the Deep Earth* (pp. 295–323), Chichester, UK: John Wiley & Sons, Ltd. https://doi.org/10.1002/9781118529492

Duesterhoeft, E., & de Capitani, C. (2013). Theriak_D: An add-on to implement equilibrium computations in geodynamic models. *Geochemistry, Geophysics, Geosystems*, 14, 4962–4967. https://doi.org/10.1002/ggge.20286

Gao, S. S., & Liu, K. H. (2014). Mantle transition zone discontinuities beneath the contiguous United States. *Journal of Geophysical Research*, 119, 6452–6468. https://doi.org/10.1002/2014JB011253

Gasparik, T. I. (2003). *Phase diagrams for geoscientists: An Atlas of the earth's interior*. Berlin, Germany: Springer; 1–462. https://doi.org/10.1007/978-3-540-38352-9

Hernández, E., Brodholt, J., & Alfè, D. (2015). Structural, vibrational and thermodynamic properties of Mg2SiO4 and MgSiO3 minerals from first-principles simulations. *Physics of the Earth and Planetary Interiors*, 240, 1–24. https://doi.org/10.1016/j.pepi.2014.10.007

Hirose, K. (2002). Phase transitions in pyrolitic mantle around 670-km depth: Implications for upwelling of plumes from the lower mantle. *Journal of Geophysical Research*, 107(B4). https://doi.org/10.1029/2001JB000597

Holland, T. J. B., Hudson, N. F. C., Powell, R., & Harte, B. (2013). New thermodynamic models and calculated phase equilibria in NCFMAS for basic and ultrabasic compositions through the transition zone into the uppermost lower mantle. *Journal of Petrology*, 54, 1901–1920. https://doi.org/10.1093/petrology/egt035

Huang, H., Tosi, N., Chang, S.-J., Xia, S., & Qiu, X. (2015). Receiver function imaging of the mantle transition zone beneath the South China Block. *Geochemistry, Geophysics, Geosystems*, 16, 3666–3678. https://doi.org/10.1002/2015GC005978

Huerta, A., Nyblade, A. A., & Reusch, A. (2009). Mantle transition zone beneath Kenya and Tanzania: More evidence for deep-seated thermal upwelling in the mantle. *Geophysical Journal International*, 177, 1249–1255. https://doi.org/10.1111/j.1365-246X.2009.04092.x

Irifune, T., Higo, Y., Inoue, T., Kono, Y., Ohfuji, H., & Funakoshi, K. (2008). Sound velocities of majorite garnet and the composition of the mantle transition region. *Nature*, 451, 814–817. https://doi.org/10.1038/nature06551

Ishii, T., Kojitani, H., & Akaogi, M. (2011). Post-spinel transitions in pyrolite and Mg2SiO4 and akimotoite–perovskite transition in MgSiO3: Precise comparison by high-pressure high-temperature experiments with multi-sample cell technique. *Earth and Planetary Science Letters*, 309, 185–197.

Jenkins, J., Cottaar, S., White, R. S., & Deuss, A. (2016). Depressed mantle discontinuities beneath Iceland: Evidence of agarnet controlled 660 km discontinuity? *Earth and Planetary Science Letters*, 433, 159–168.

Kennet, B. L. N. (1983). *Seismic wave propagation in stratified media by B. L. N. Kennett*. Canberra, ACT: Cambridge University Press.

Kind, R., Kosarev, G. L., & Petersen, N. V. (1995). Receiver functions at the stations of the German Regional Seismic Network (GRSN). *Geophysical Journal International*, 121, 191–202. https://doi.org/10.1111/j.1365-246X.1995.tb03520.x

Langston, C. A. (1979). Structure under Mount Rainier, Washington, inferred from teleseismic body waves. *Journal of Geophysical Research*, 84(B9), 4749–4762. https://doi.org/10.1029/JB084iB09p04749

Lawrence, J. F., & Shearer, P. M. (2006). A global study of transition zone thickness using receiver functions. *Journal of Geophysical Research*, 111, B06307. https://doi.org/10.1029/2005JB003973

Liu, X., Xiong, Z., Chang, L., He, Q., Wang, F., Shieh, S. R., … Zhang, L. (2016). Anhydrous ringwoodites in the mantle transition zone: Their bulk modulus, solid solution behaviour, compositional variation, and sound velocity feature. *Solid Earth Sciences*, 1, 28–47. https://doi.org/10.1016/j.sesci.2015.09.001

Lyubetskaya, T., & Korenaga, J. (2007). Chemical composition of Earth's primitive mantle and its variance: 1. Method and results. *Journal of Geophysical Research*, 112, B03211. https://doi.org/10.1029/2005JB004223

Maguire, R., Ritsema, J., & Goes, S. (2017). Signals of 660 km topography and harzburgite enrichment in seismic images of whole-mantle upwellings. *Geophysical Research Letters*, 44, 3600–3607. https://doi.org/10.1002/2017GL073120

Mookherjee, M., Karki, B. B., Stixrude, L., & Lithgow-Bertelloni, C. (2012). Energetics, equation of state, and elasticity of NAL phase: Potential host for alkali and aluminum in the lower mantle. *Geophysical Research Letters*, 39, L19306. https://doi.org/10.1029/2012GL053682

Morgan, W. J. (1972). Plate motions and deep mantle convection. In R. Shagam, R. B. Hargraves, W. J. Morgan, F. B. Van Houten, C. A. Burk, H. D. Holland & L. C. Hollister (Eds.), *Studies in earth and space sciences*. GSA Memoirs 132, 7–22. Boulders, CO: Geological Society of America. https://doi.org/10.1130/MEM132

Shen, Y., & Blum, J. (2003). Seismic evidence for accumulated oceanic crust above the 660-km discontinuity beneath southern Africa.

Geophysical Research Letters, 30, 1925. https://doi.org/10.1029/2003GL017991, 18

Shen, X., Yuan, X., & Li, X. (2014). A ubiquitous low-velocity layer at the base of the mantle transition zone. *Geophysical Research Letters*, 41, 836–842. https://doi.org/10.1002/2013GL058918

Shorttle, O., Mavlennan, J., & Lambart, S. (2014). Quantifying lithological variability in the mantle. *Earth and Planet Science Letters*, 395, 24–40.

Sinogeikin, S. V., & Bass, J. D. (2002). Elasticity of Majorite and a Majorite-Pyrope solid solution to high pressure: Implications for the Transition Zone. *Geophysical Research Letters*, 29, 1017. https://doi.org/10.1029/2001GL013937

Sinogeikin, V. S., Bass, J. D., Kavner, A., & Jeanloz, R. (1997). Elasticity of natural majorite and ringwoodite from the catherwood meteorite. *Geophysical Research Letters*, 24, 3265–3268. https://doi.org/10.1029/97GL03217

Stammler, K., Kind, R., Petersen, N., Korsarev, G., Vinnik, L., & Qiyuan, L. (1992). The upper mantle discontinuities: Correlated or anticorrelated? *Geophysical Research Letters*, 15, 1563–1566. https://doi.org/10.1029/92GL01504

Stixrude, L., & Lithgow-Bertelloni, C. (2011). Thermodynamics of mantle minerals - II. Phase equilibria. *Geophys Journal International*, 184, 1180–1213.

Stixrude, L., & Lithgow-Bertelloni, C. (2012). Geophysics of chemical heterogeneity in the Mantle. *Annual Review of Earth and Planetary Sciences*, 40, 569–595. https://doi.org/10.1146/annurev.earth.36.031207.124244

Tauzin, B., & Ricard, Y. (2014). Seismically deduced thermodynamics phase diagrams for the mantle transition zone. *Earth and Planetary Science Letters*, 401, 337–346. https://doi.org/10.1016/j.epsl.2014.05.039

Vinnik, L. P. (1977). Detection of waves converted from P to SV in the mantle. *Physics of the Earth and Planetary Interiors*, 15, 39–45. https://doi.org/10.1016/0031-9201(77)90008-5

Vinnik, L., & Farra, V. (2006). S velocity reversal in the mantle transition zone. *Geophysical Research Letters*, 33, L18316. https://doi.org/10.1029/2006GL027120

Vinnik, L. P., Foulger, G. R., & Du, Z. (2005). Seismic boundaries in the mantle beneath Iceland: A new constraint on temperature. *Geophysical Journal International*, 160, 533–538. https://doi.org/10.1111/j.1365-246X.2005.02529.x

Vinnik, L., Kosarev, G., & Petersen, N. (1996). Mantle transition zone beneath Eurasia. *Geophysical Research Letters*, 23, 1485–1488. https://doi.org/10.1029/96GL01261

Xu, W., Lithgow-Bertelloni, C., Stixrude, L., & Ritsema, J. (2008). The effect of bulk composition and temperature on mantle seismic structure. *Earth and Planetary Science Letters*, 275, 70–79. https://doi.org/10.1016/j.epsl.2008.08.012

Yu, Y. G., Wentzcovitch, R. M., Tsuchiya, T., Umemoto, K., & Weidner, D. J. (2007). First principles investigation of the postspinel transition in Mg2SiO4. *Geophysical Research Letters*, 34, L10306. https://doi.org/10.1029/2007GL029462

Zhu, L., & Kanamori, H. (2000). Moho depth variation in southern California from teleseismic receiver functions. *Journal of Geophysical Research*, 105(B2), 2969–2980. https://doi.org/10.1029/1999JB900322

SUPPORTING INFORMATION

Additional supporting information may be found online in the Supporting Information section at the end of the article.

Figure S1. Equilibrium phase diagram for primitive mantle composition as proposed by Sun and McDonough (1989) calculated using the database of Holland et al. (2013). Molar abundances in bulk composition used for the calculation are: Si, 38.16; Al, 4.44; Fe, 5.71; Mg, 47.88; Ca, 3.210; Na, 0.590; O, 140.075. Abbreviations and assemblage labels are the same as in Figure 1. Phase relations are almost identical to Figure 1; however, slightly shifted towards lower temperatures.

Figure S2. Relation between seismic velocities (vs and vp) and depth along 1,350 (blue), 1,450 (green), 1,550 (red), and 1,650 (pink) adiabates respectively (Figure 1). Assumed composition is again the one used for the calculation of Figures 1–5 in the main text. Pressures in Figure 3b are converted to depths by vertical integration of densities along the 1,350 adiabat (Figure 3a). Hence, we assume horizontal pressure equilibrium.

Figure S3. Comparison of 1D synthetic receiver functions of the derived velocity model along the 1,650°C adiabat using three different Gaussian factors, $a = 3$ (green), $a = 2$ (light blue), $a = 1$ (dark blue). It is evident that with decreasing Gaussian factor (increasing smoothing), the complex 660-discontinuity becomes oversimplified. In the cases $a = 3$ and $a = 2$, the main phase transition at the 660 discontinuity is recovered, followed by a weaker signal representing a velocity gradient beneath the 660. In the case $a = 1$, the maximum amplitude of the 660 discontinuity shifts to larger delay times because of the smoothing effect. Orange dotted line indicates the depth of the largest gradient in the velocity model, i.e., the theoretical 660 discontinuity.

Figure S4. Comparison of 1D synthetic receiver functions in the range of the Mantle Transition Zone using the derived models for the 1,350°C adiabat (blue) and 1,650°C adiabat (red) with (solid lines) and without (stippled lines) multiples from arbitrarily chosen and oversimplified lithospheric discontinuities (Moho at 35 km with $\rho = 2,800$ kg/m^3, $Vs = 3.8$ km/s and $Vp = 6.6$ km/s, lithosphere–asthenosphere boundary at 135 km depth with $\rho = 3,300$ kg/m^3, $Vs = 4.6$ km/s and $Vp = 8.0$ km/s). We can conclude that multiples originating from lithospheric structure do not compromise the interpretation of the mantle transition zone (MTZ) discontinuities and assumingly lie within or below the expected noise levels.

Figure S5. Equilibrium phase diagram for a composition consisting of 80% primitive mantle (Lyubetskaya and Korenaga, 2007) and 20% pyroxenite (MIX1G, Hirschmann et al., 2003). Molar abundances in bulk composition used for the calculation are: Si, 38.68; Al, 5.92; Fe, 5.70; Mg, 44.68; Ca, 4.16; Na, 0.86; O, 141.210. Abbreviations and assemblage labels are the same as in Figure 1. The critical assemblage boundaries in the MTZ are shifted towards lower temperatures by about 130°C.

Figure S6. Equilibrium phase diagram for primitive mantle (Lyubetskaya and Korenaga, 2007) calculated using the database of Stixrude and Lithgow-Bertelloni (2011) and Theriak-Domino software (De Capitani and Petrakakis, 2010). fer, ferrite; st, stishovite; Other abbreviations and assemblage labels are the same as in Figure 1. Stippled coloured lines correspond to same adiabats (isentropes) as in Figure 1. Note that the 1,650 adiabat cuts much less into the grt + periclase stability field in the lower MTZ. Hence, the associated velocity anomaly (Figure S9) is somewhat less pronounced as compared to our model.

Figure S7. Density of primitive mantle (Lyubetskaya and Korenaga, 2007) as predicted by the database of Holland et al. (2013) (a) and

Stixrude and Lithgow-Bertelloni (2011) (b) along the four reference adiabats (Figures 1 and S6). Colour code is the same as in these figures. Stippled grey line corresponds to the PREM (Dziewonski and Anderson, 1989).

Figure S8. Elastic moduli of primitive mantle (Lyubetskaya and Korenaga, 2007) as predicted by the database of Holland et al. (2013) together with our calculation scheme for shear modulus incorporated in Theriak-Domino software (Figures (a) and (b)) and by the database of Stixrude and Lithgow-Bertelloni (2011) (Figures (c) and (d)) along the four reference adiabats (Figure 1 and S6). Colour code is the same as in these figures. Figures (a) and (c) correspond to shear moduli and Figures (b) and (d) to bulk moduli respectively. Strippled grey line shows the PREM (Dziewonski and Anderson, 1989).

Figure S9. Seismic velocities of primitive mantle (Lyubetskaya and Korenaga, 2007) as predicted by the database of Holland et al. (2013) together with our calculation scheme for shear modulus incorporated in Theriak-Domino software (Figures (a) and (b)) and by the database of Stixrude and Lithgow-Bertelloni (2011) (Figures (c) and (d)) along the four reference adiabats (Figures 1 and S6). Colour code is the same as in these figures. Figures (a) and (c) correspond to V_s and figures (b) and (d) to V_p respectively. Stippled grey line shows the PREM (Dziewonski and Anderson, 1989).

Table S1. Comparisons between modelled and experimental shear moduli μ of majoritic garnet and periclase. Number in parenthesis represents uncertainties in the last digit.

Data S1. Calculating seismic velocities.